INTERNATIONAL JOURNAL OF
COASTAL, OFFSHORE & ENVIRONMENTAL ENGINEERING
IJCOE Vol.10/No. 2/Spring 2025 (7-15)

Available online at: www. Ijcoe.org

Long-range Power Density Profiling Measurement Using Coastal Acoustic Tomography (Study area: Persian Gulf)

Mehran Sadeghi Delooee[1], Reza Alimardani[2*],Hossein Mousazadeh[3], Masoud Bahreinimotlagh[4], Reza Roozbahani[5], Mortaza Eftekari[6], Mohammed Basel AlSawaf[7], Sayyed Ahmad Sajjadi[8], Ashkan Farokhnia[9], Reza Hosseinzadeh Asl[10], Ali Davaei[11]

1 Department of Mechanical Engineering of Biosystems, University of Tehran, Tehran, Iran
*2 *Department of Mechanical Engineering of Biosystems, University of Tehran, Tehran, Iran (r.mardani@ut.ac.ir)*
3 Department of Mechanical Engineering of Biosystems, University of Tehran, Tehran, Iran
4 Water Research Institute, Tehran, Iran
5 Water Research Institute, Tehran, Iran
6 Water Research Institute, Tehran, Iran
7 Faculty of Engineering Department of Civil and Environmental Engineering, Kitami Institute of Technology, Kitami, Japan
8 Department of Mechanical Engineering, Iran University of Science and Technology, Tehran, Iran
9 Department of Energy, Institute of Science and High Technology and Environmental Science, Graduate University of Advanced Technology, Kerman, Iran
10 College of Agricultural Engineering and Technology, University of Tehran, Iran
11 Department of Computer Engineering, South Tehran Branch, Islamic Azad University, Tehran, Iran

ARTICLE INFO

Article History:
Received : 21 Feb 2024
Accepted : 10 Jun 2025

Keywords:
Tidal stream turbine
Layered current velocity
Persian Gulf
CAT
Inverse Problem

ABSTRACT

Prior to the design and installation of tidal stream turbines, a thorough understanding of coastal hydrodynamic parameters, such as power density, is essential. The accurate estimation of current velocity is a key component in power density calculations. Acoustic Tomography (AT), as a robust remote sensing technique, is widely employed to measure currents velocities across various water layers. This methodology relies on recording the travel time of acoustic waves propagating through the water layers, followed by the solution of the associated AT inverse problem. This study conducted a reciprocal sound transmission experiment in the Persian Gulf, employing two 10-kHz Coastal Acoustic Tomography (CAT) stations situated 3 km apart, and submerged 6 meters beneath the water surface. The five-layer structures of the range-averaged current in the vertical section were reconstructed through regularized inversion of the travel time data for two rays. The regularized inversion revealed a maximum velocity of 0.89 m/s within layer 3 (20-30 m depth). Notably, velocity inversion errors across all five layers (1-5) remained negligible, ranging from 0.006 to 0.014 m/s, compared to the observed velocity variation. Further analysis of the velocity histogram indicated that the dominant current speeds at the site fell within the range of 0.1-0.5 m/s, falling short of the standard economic threshold of 1 m/s for tidal energy conversion. These findings demonstrate the potential of CAT to accurately profile coastal current velocities.

1. Introduction

There are several substitutes available to reduce greenhouse gas (GHG) emissions from energy systems that can meet the global energy demand. Renewable energy stands as a promising alternative, which has great potential for climate change mitigation, social and economic development, providing a safe source of energy, and reducing environmental impact (Thiébaut et al., 2020).

The oceans, which cover more than two-thirds of the earth, have significant amounts of energy in the form of waves, tidal currents (Jahromi, 2024; khoshkholgh, 2023), as well as heat and salinity gradients (Bahaj, 2013). Tidal stream energy, or marine hydrokinetic energy (MHKE), attracts significant attention compared to other forms of ocean energy due to its reliable and predictable nature (Radfar et al., 2017). The life cycle of a tidal energy typically involves three main stages: (1) design and construction, (2) installation, and (3) operation and maintenance.

Monitoring and measuring the flow field, particularly the vertical variation of current velocity, is crucial throughout the life cycle of a tidal energy converter. During Stage 1, this information is paramount for tidal energy converter developers, as many industry-standard flow characterization metrics depend on descriptions of the underlying mean flow (Sellar & Wakelam, 2018; Thiébaut et al., 2020). During Stage 2, thorough resource assessment becomes critical. This process ensures the safe utilization and efficient operation of tidal stream turbines (Gunawan et al., 2014).

As stated, the resource assessment, specifically measuring power density, is a key action in developing and installing tidal stream turbines. While the primary parameter assessed is current velocity, there is no significant difference between resource assessments of different tidal stream energy converters (turbines and kites).

Acoustic Tomography (AT) has evolved as a valuable tool for monitoring coastal waters, without disrupting activities like fishing and shipping. This technology uses a special technique that analyzes travel times of acoustic signals in water to extract the parameters of an aquatic medium (including sound speed, current velocity, and temperature) on a large scale area. A typical AT device (Figure 1 b) is comprised of a pair of acoustic transducers and processing units (Kaneko et al., 2020).

This study aims to reconstruct high-resolution vertical profiles of current velocity. Many researchers have mapped vertical profiles of current velocity and water temperature using AT and compared their results with Acoustic Doppler Current Profiler (ADCP), Acoustic Doppler Velocimeter (ADV), and CTD measurements.

Taniguchi et al. (2013) employed AT to profile the flow velocity of the Kuroshio Current in southeast Taiwan, comparing their results with data from a moving ADCP. They used the explicit solution and regularized inversion to estimate the current velocity. Their analysis found a high degree of consistency between the AT and ADCP measurements, further validating the accuracy of AT for measuring current velocities in complex ocean environments.

Li et al. (2017) successfully utilized AT to map the complex internal flow structure within a circular multidirectional wave/current basin. They divided the water column into five layers and estimated the layered current velocity by solving the regularized inverse problem. Notably, their AT results showed close agreement with measurements from an Acoustic Doppler Velocimeter (ADV), demonstrating the robustness of AT for measuring flow velocity.

Syamsudin et al. (2017) deployed two CAT devices in the Bali Strait, to measure the velocity and temperature of tidal currents across five vertical layers. Their results, when compared to data from an ADCP, showcased a high degree of agreement, demonstrating the accuracy and effectiveness of AT for measuring these parameters.

Syamsudin et al. (2019) employed the one-way AT in the Lombok Strait, to map the temperature profiles of internal solitary waves across four distinct layers. They compared their reconstructed temperatures with data from a Conductivity-Temperature-Depth (CTD) sensor, finding an excellent match between the AT and CTD measurements.

Huang et al. (2020) utilized CAT to measure high-resolution water temperature profiles across four layers within Thousand-Island Lake, Hangzhou, China. This technique, particularly relevant for environmental monitoring in the lake, achieved good agreement with the CTD data.

Taniguchi et al. (2021) investigated the effectiveness of AT in capturing high-frequency fluctuations in tidal currents. Their study successfully demonstrated agreement between AT's path-averaged current estimates and hourly ADCP data. Notably, AT was able to detect these fast variations which eluded the ADCP, highlighting its potential to enhance the reconstruction of velocity fields through inversion or data assimilation methods. These results show the high accuracy of AT and prove its feasibility for measuring tidal current velocity. Thus, no further comparison with the ADCP measurement is needed.

Kawanishi et al. (2015) pioneered the use of AT to assess tidal energy potential in the Nekosto Strait of Japan, with a maximum water depth of 100 meters. Their study estimated a peak flow velocity of 1 m/s across the strait, translating to a potential power output of 40 MW and an average power density of 0.5 kW/m². While this marked the first application of AT for calculating power density, the analysis exclusively focused on depth-averaged values, leaving room for future investigations into vertical variations in power potential.

This study uses AT to map vertical profiles of current velocity in the Persian Gulf, employing a regularized inverse problem to solve for velocity values. By analyzing these velocities, we can extract power density, a crucial parameter for identifying potential tidal energy sites. Our research distinguishes itself by calculating the layered power density (detailed in section 3.5). This innovative approach facilitates the determination of the optimal installation depth for tidal stream turbines, maximizing their energy extraction potential.

2. Material and Methods

2.1. Experimental settings

In this study, two 10 kHz CAT stations operating were deployed in the Persian Gulf, Iran (Figure 1a). Each station (S1 and S2) transmitted acoustic signals to its counterpart at 1-minute intervals, separated by a distance of 3 km and a depth of 6 meters from the water surface. Notably, the seabed exhibited a smooth topography with a consistent depth of 60 meters between the stations (Figure 1b). To complement the AT measurements, concurrent data on water temperature and salinity (CTD) was collected throughout the water column.

In noisy aquatic mediums such as gulfs, coasts, and shallow water of rivers, a particular method is required for transmitting and processing sound, which hinders signal attenuation. It has been proven that signal

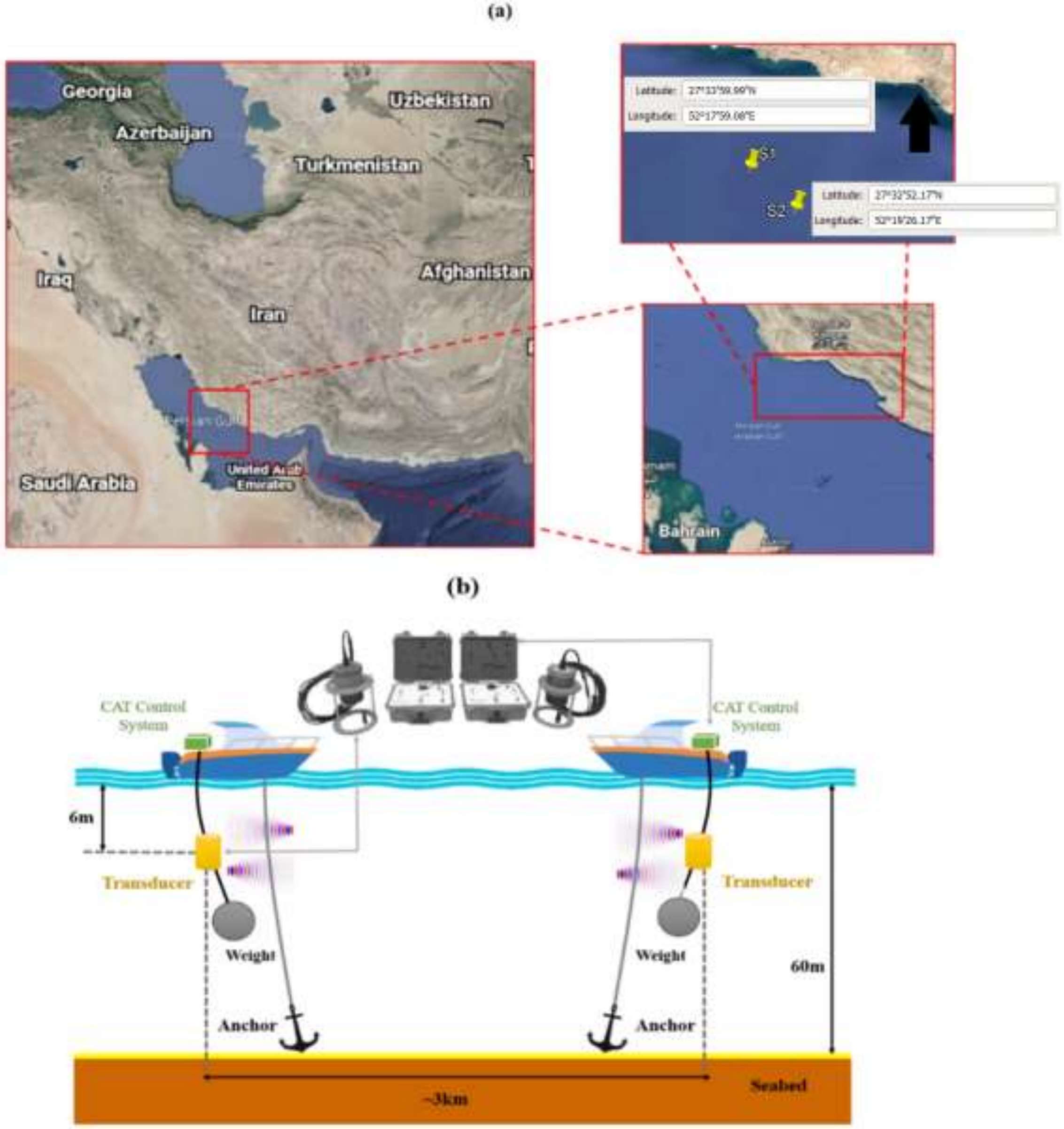

Figure 1. Sound transmission: (a) geographical location, and (b) schematic of the experimental arrangement and the components of a typical CAT system

modulation with an M-sequence and taking the cross-correlation of received signals is an efficient method (Bahreinimotlagh et al., 2020).

Table 1 shows the characteristics of M-sequence modulated signals that were transmitted reciprocally in this experiment.

Table 1. Characteristics of the reciprocal sound signals

M-sequence order	12
Carrier cycles per digit	1023
Source Level	190 dB re 1 μPa at 1 m

Examining the peak values in the correlation plots (also known as signal-to-noise ratio or SNR) reveals the arrival times of different acoustic rays. While the highest peak corresponds to the first ray, subsequent arrivals can be identified by analyzing smaller peaks within specific time windows after the initial peak. This process extracts both the arrival times and their corresponding travel times, essential for calculating range-averaged current values.

2.2. Range-independent ray simulation

Ray simulation, a fundamental step in the CAT implementation, utilizes the site-specific CTD data to theoretically model acoustic ray paths. In coastal environments, the ray-tracing method simulates sound propagation by considering only refraction using Snell's rule (Kaneko et al., 2020). In this study, we employed ray-tracing to simulate sound transmission between stations S1 and S2. Ray simulation provides the possible successfully transmitted rays (called Eigen rays), which are valuable in arrival peaks identification procedure and regularized inverse problem solution.

2.3. Range-averaged current (RAC) and lowpass filter

Considering a reciprocal sound transmission between two stations (S1→S2 and S2→S1) with a distance of L, the corresponding travel times t_1 and t_2 can be calculated by taking a path integral, as Eqs. 1 and 2 (Kaneko et al., 2020):

$$t_1 = \int_{\Gamma^+} \frac{ds}{C+v} \approx \frac{L}{C_m + V_m} \tag{1}$$

$$t_2 = \int_{\Gamma^-} \frac{ds}{C-v} \approx \frac{L}{C_m - V_m} \tag{2}$$

where $\Gamma^+$and $\Gamma^-$are the ray paths, ds is the arch length element along the refracted ray, C is the sound speed, and v is the current velocity. On the right side of the Eqs. 1 and 2, C_m and V_m represent the section-averaged sound speed and current velocity.

The range-averaged velocity, or more often referred to as range-averaged current (RAC), in the vertical cross-section of the two stations is calculated by solving Eqs. (1) and (2) which yields Eq. (3):

$$V_m = \frac{C_0^2}{2L} \Delta t \tag{3}$$

where $\Delta t = t_2 - t_1$, is the differential travel time, and C_0 is the reference sound speed.

The RAC time series often exhibits significant high-frequency components, which are seen as severe fluctuations. To address this issue, we implemented a 10-minute Blackman window low-pass filter, effectively smoothing the RAC time-series. Therefore, modified differential times were calculated using Eq. (4) to account for these filtering-induced changes."

$$\Delta t' = V_m' \frac{2L}{C_0^2} \tag{4}$$

where V_m' and $\Delta t'$ are the lowpass filtered range-averaged velocity and modified differential time, respectively.

2.4. Regularized inversion

In case M acoustic rays pass through N layers, the travel time of the i-th ray along and against the current (t_i^+ andt_i^-) equals to:

$$t_i^{\pm} = \sum_{i=1}^{N} \frac{l_{ij}}{(c_j \pm u_j)} \tag{5}$$

In Eq. (5) c_j is the path-averaged sound speed, u_j is the current velocity for the j-th layer, and l_{ij} is the arc length of the i-th ray passing through the j-th layer (Li, 2018). Since the current velocity is significantly smaller than the sound speed ($u \ll c$), the differential travel times (DTTs) can be formulated as Eq. (6), and it could be shown in its matrix notation (Eq. 7).

$$\Delta t_i = (t_i^+ - t_i^-) = -2 \sum_{i=1}^{N} \frac{l_{ij} u_j}{c_j^2} \tag{6}$$

$$\begin{bmatrix} \Delta t_1 \\ \Delta t_2 \\ \vdots \\ \Delta t_M \end{bmatrix} = \begin{bmatrix} -2\frac{l_{11}}{c_1^2} & -2\frac{l_{12}}{c_2^2} & \cdots & -2\frac{l_{1N}}{c_N^2} \\ -2\frac{l_{21}}{c_1^2} & -2\frac{l_{22}}{c_2^2} & \cdots & -2\frac{l_{2N}}{c_N^2} \\ \vdots & \vdots & \ddots & \vdots \\ -2\frac{l_{M1}}{c_1^2} & -2\frac{l_{M2}}{c_2^2} & \cdots & -2\frac{l_{MN}}{c_N^2} \end{bmatrix} \cdot \begin{bmatrix} u_1 \\ u_2 \\ \vdots \\ u_N \end{bmatrix} \tag{7}$$

Eq. (7) can be generalized as Eq. (8), in which y is the DTTs matrix, E is the coefficients matrix (sound speed and arc length of each ray in each layer), x is the layered current velocity matrix, and n is the error matrix.

$$y = Ex + n \tag{8}$$

There are several approaches to solve the inverse problem (Eq. 8). The classic algebra (least-squares) is not recommended for solving the acoustic tomography inverse problem, owing to the ill-posed nature of the problem, which leads to an unstable solution. To overcome the challenges associated with ill-posedness in the inverse problem, we employ a regularization technique (Eq. (9) and Figure 2). This approach effectively mitigates solution instability and yields an accurate and physically meaningful reconstruction of the current velocity field (Syamsudin et al., 2019).

$$\begin{aligned} J = n^T n + \lambda x^T H^T H x \\ = (y - Ex)^T (y - Ex) \\ + \lambda x^T H^T H x \end{aligned} \tag{9}$$

$$\hat{x} = (E^T E + \lambda H^T H)^{-1} E^T y \tag{10}$$

where λ is the Lagrange multiplier, and it is determined by minimizing the squared residuals considering a predetermined value. H is the regularization matrix, which is made from a second-order derivative operator $\frac{\partial^2 \mathrm{x}}{\partial \mathrm{z}^2}$.

This matrix is used to smooth the solution by applying a moving average to three consecutive layers (Syamsudin et al., 2017).

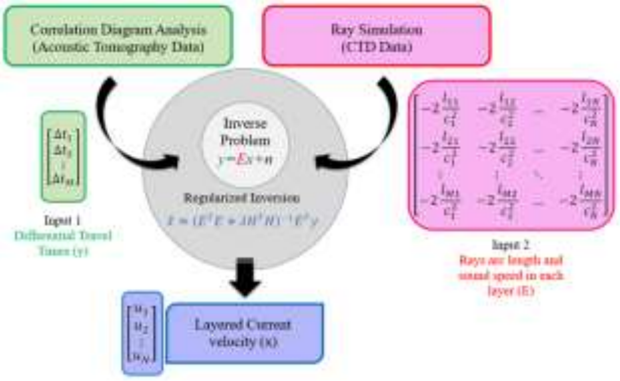

Figure 2. Components of a regularized inverse problem

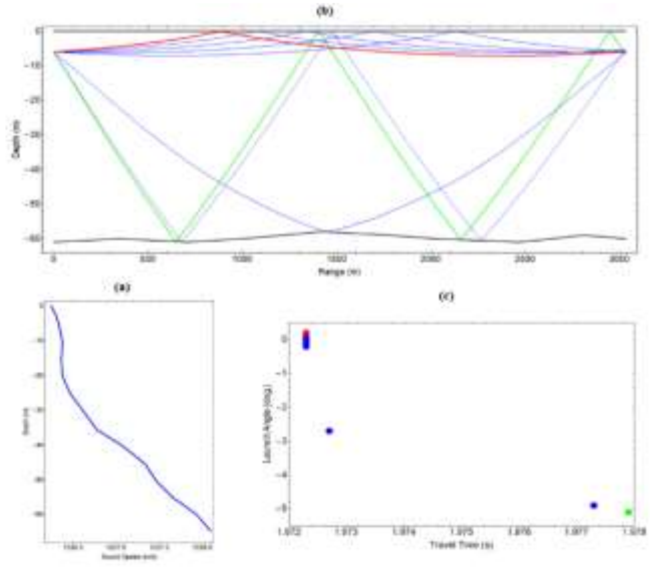

Figure 3. Results of the range-independent ray simulation: (a) Sound speed profile, (b) Transmitted Eigen rays between S1 and S2 (marked by red and green curves), (c) Rays travel times

$$\int_{-D}^{0}\left(\frac{\partial^2 \mathrm{x}}{\partial \mathrm{z}^2}\right)^2 dz = \sum_{i=1}^{M}(x_{i-1}-2x_i + x_{i+1})^2 = x^T H^T H x \qquad (11)$$

where D is the seabed depth. Considering 5 horizontal layers for a vertical slice, the regularization matrix is expressed by Eq. (12).

$$H = \begin{bmatrix} -2 & 1 & 0 & 0 & 0 \\ 1 & -2 & 1 & 0 & 0 \\ 0 & 1 & -2 & 1 & 0 \\ 0 & 0 & 1 & -2 & 1 \\ 0 & 0 & 0 & 1 & -2 \end{bmatrix} \qquad (12)$$

Inversion uncertainty is formulated as Eq. (13), where $\langle nn^T \rangle$ is the expected variance of differential travel times. Velocity inversion error can be estimated by Eq. (14).

$$P = (E^T E + \lambda H^T H)^{-1} E^T \langle nn^T \rangle E (E^T E + \lambda H^T H)^{-1} \qquad (13)$$

$$V_{error} = diagonal(\sqrt{P_{\Delta t}}) \qquad (14)$$

2.5. Power density

Power per unit area is called power density (PD) and calculated by Eq. (15), where ρ ($1025 kg/m^3$) is the seawater density, and V is the current velocity.

$$PD = \frac{P}{A} = \frac{1}{2}\rho V^3 \qquad (15)$$

3. Results and discussion

This section delves into the analysis of the AT data, divided into two key parts: (a) Processing and Interpretation: This covers ray simulation, arrival peak identification, range-averaged current calculation, and inversion results, and (b) Site Characterization: This focuses on assessing the site's velocity status through vertical profiles, velocity histograms, and power density estimation.

3.1. Ray simulation

Initially, the CTD data and Mackenzie's equation were used to calculate the sound speed profile. Then, the ray simulation was performed to determine the Eigen rays transmitted between two stations. The sound speed profile (Figure 3 a) exhibits slight change from the surface to the seabed. Regarding ray simulation results and correlation diagrams, two peaks are identified. These peaks correspond to the first (Ray 1, red-ray in Figure 3b) and second (Ray 2, green-ray in Figure 3b) Eigen rays, representing refracted surface-reflected (RSR) and surface-reflected bottom-reflected (SRBR) paths, respectively. Their reference travel times and ray arch lengths within each layer are summarized in Table 2.

3.2 Arrival peak identification

Signal processing of the raw AT data yielded correlation diagrams (travel time-SNR). Since two rays were successfully transmitted, we needed to identify two arrival peak points. The first peak was extracted using the largest peak method with an SNR threshold of 5. Ray simulation data (Table 2) predicted the second peak to occur about 5.5 ms later. Therefore, a 5-ms search window with a lower SNR threshold of 3 was used to identify the second peak (Figure 4a). Figure 4b presents the correlation diagrams and the identified peak points for both simultaneous signals.

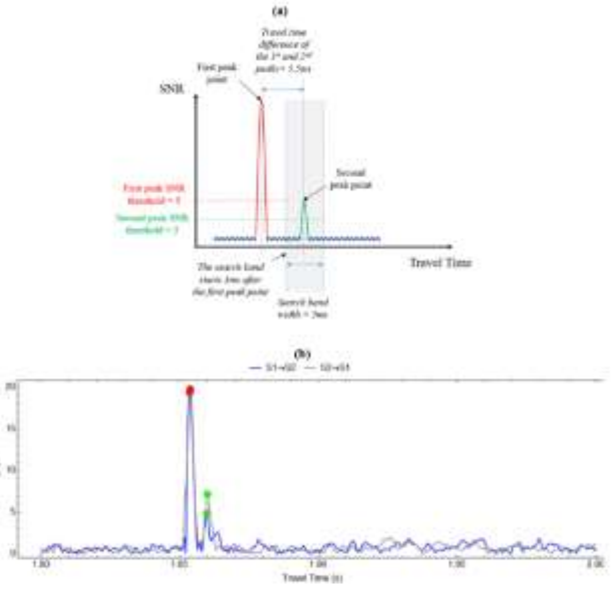

Figure 4. Arrival peak identification, (a) SNR thresholds and the search band, and (b) The correlation diagram of reciprocal sound transmission and the identified peaks

Table 2. Layered arch length and reference travel time of the transmitted eigen rays

Ray No.	Travel time	Ray length in:				
		Layer 1	**Layer 2**	**Layer 3**	**Layer 4**	**Layer 5**
Ray 1 (RSR)	1.97231	3029.9	0	0	0	0
Ray 2 (SRBR)	1.9779	490.1	475.8886	480.0697	495.2206	1098.3

Applying the same procedure to the entire dataset generated a layered view of all correlation diagrams in Figure 5, where the first (red) and second (green) arrival peaks for each measurement are clearly marked. As expected, the first surface-reflected peaks exhibit higher SNR levels (15-20) due to minimal energy loss. In contrast, the second peaks, which involve multiple interactions with the seabed, show significantly lower SNR (5-10) due to signal strength. Additionally, Figures 5c and 5d reveal that the estimated ray travel times are consistently between 1.85 and 1.92 seconds.

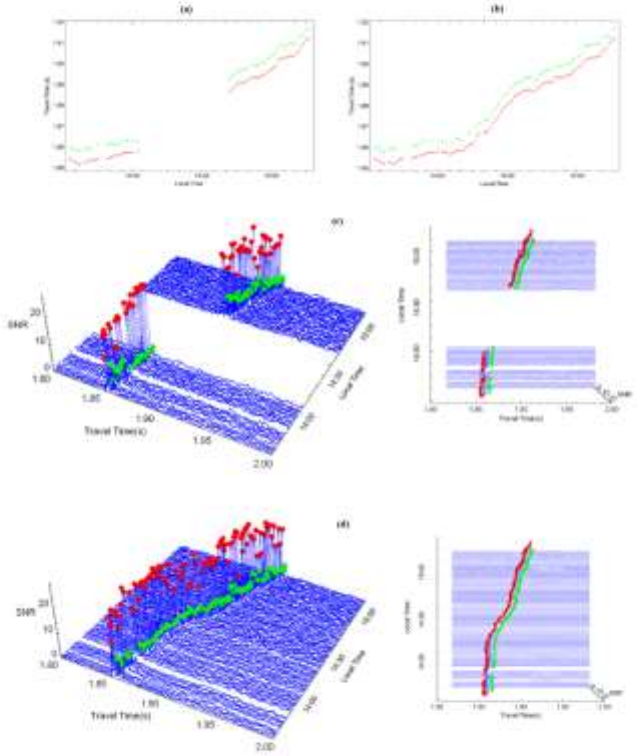

Figure 5. Stack plots of correlation diagrams with the 1st and 2nd peaks marked red and green respectively: (a) S1→S2, (b) S2→S1, and their corresponding travel

Figure 5a reveals a data gap between 14:03 and 14:40, corresponding to a loss of signals. This occurred due to a temporary battery malfunction in the CAT station during the experiment. We carefully evaluated the impact of this missing data and found it to have a negligible effect on the following calculations.

3.3 Range-averaged current (RAC)

Range-averaged current (RAC) values were calculated using Equation (3) based on the differential travel time between the first and second arrival peaks. A Blackman window low-pass filter with a 10-minute cutoff frequency was applied to smooth the RAC time series (red and green curves in Figure 6).

The RAC values reconstructed using the first and second peaks exhibit notable differences. This likely originates from the distinct paths traversed by each ray: the first exclusively within the first layer, while the second interacted with all five layers of the water column (Figure 7). This observation suggests a clear disparity between the surface current regime (layer 1) and the whole vertical slice current regime.

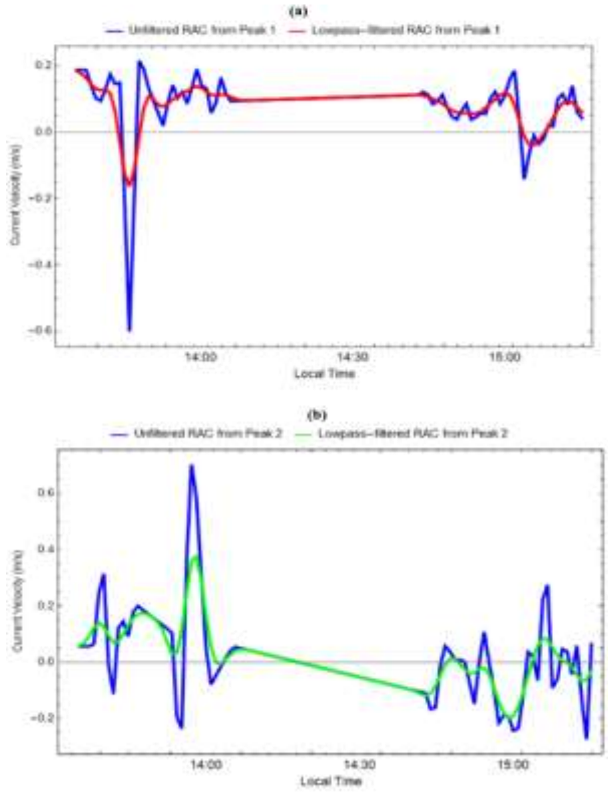

Figure 7. Current velocity calculated by regularized inversion: The highlighted regions show the before and after the battery malfunction time which were used to investigate the current histogram and power density in section 3.5

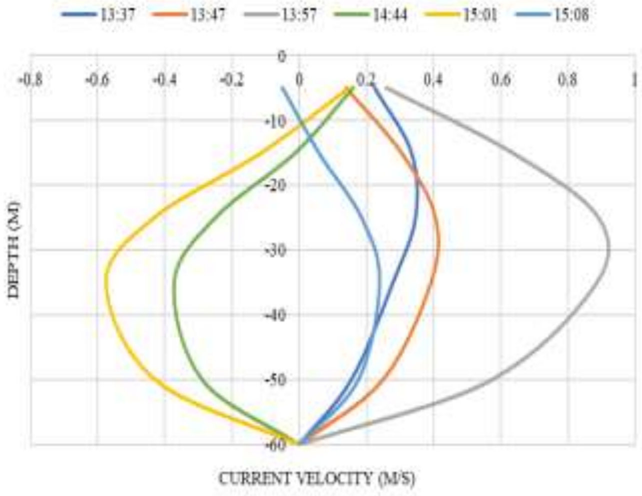

Figure 8. Current velocity vertical profiles in 6 different instants

3.4 Inversion results and current velocity profiles

Solving the regularized inverse problem with adjusted travel times and ray simulation data (Figure 3) revealed the current velocity distribution within five layers (0-10, 10-20, 20-30, 30-40, and 40-60 m) (solid lines in Figure 8). However, these velocity values must be corrected regarding the angle between the transmission line and the current dominant direction (α) which was estimated to be 54° in this research (Appendix).

The corrected velocity values are shown as dashed lines in Figure 8. The maximum current velocity of 0.89 m/s occurred in layer 3 at 13:57. At this specific time, the velocities in other layers were: 0.26 m/s (layer 1), 0.63 m/s (layer 2), 0.88 m/s (layer 4), and 0.57 m/s (layer 5). Table 3 presents the inversion error for each layer. Analyzing these values alongside the range of velocities observed in the data, we can confidently conclude that the inversion error is negligible, indicating robust and accurate velocity estimation.

Figure 9 clearly reveals that layers 3 and 4 have the most potential for exhibiting significantly higher velocity values compared to the other layers. To quantify the similarity in velocity behavior across layers, we calculated the Root Mean Squared Error (RMSE) of the velocity time series for each layer pair (Table 4). This analysis reveals a particularly low RMSE of 0.08 between layers 3 and 4, indicating that their velocity profiles are nearly identical.

”

3.5 Velocity histogram and Power density (PD)

Focusing on layers 3 and 4, we analyzed only the highlighted sections in Figure 8 to gain clearer insights into the site's typical current velocity status and power density values. The sign of velocity (+ or -) indicates the current direction, but since it is not of high importance, the absolute value of velocities was taken into account.

The velocity histogram (Figure 9 a) shows that the site predominantly experiences current speeds between 0.1 and 0.5 m/s. Sites with practical current velocities greater than 1 m/s are economically viable, but the current in this site during the experiment does not satisfy this limit. Therefore, this site likely wouldn't support sufficient power generation for in-stream tidal turbines. This conclusion aligns with the power density (PD) analysis. While peak PD values reach 350 and 100 W/m² in sections A and B (Figure 9b and 9c), respectively, the average PD remains significantly lower at 42 and 14 W/m², respectively.

These findings emphasize the importance of extended measurement periods to capture temporal variations in current velocity and considering more efficient tidal energy conversion systems, such as tidal kites developed by Minesto. It is also claimed that due to the moving nature of this energy conversion method, the current velocity can increase up to ten times (Roberts et al., 2016). The tidal kite system operates typically at mid-depth. Often described as a "flying" kite with a turbine and generator attached underneath, it traces a lying figure-eight path nearly perpendicular to the tidal flow.

This paper and the research conducted by (Kawanishi et al., 2015) indicate the capability of the AT technique in measuring power density for tidal energy potential assessment. However, the calculation of layered power density in this paper enables us to determine the best installation depth for tidal stream turbines.

4. Conclusion

Utilizing two 10-kHz CAT stations, this study assessed the tidal stream energy potential in the Persian Gulf, Iran, by mapping velocity and energy profiles through the regularized inverse problem. Reciprocally transmitted acoustic rays with measured arrival times were used to calculate range-averaged current (RAC) values, crucial for assessing tidal stream energy potential. Differences in RAC values between rays 1 and 2, likely due to distinct travel paths, necessitated smoothing the time series with a low-pass filter. This smoothed data then served as input for the regularized inverse problem, enabling the reconstruction of velocity profiles within a 5-layer vertical slice.

Layer 3 experienced the maximum velocity with a value of 0.89 m/s. The accurate evaluation of velocity profiles and considering RMSE between layers indicated that layers 3 and 4 are very similar and have a higher potential than others.

Further analysis of the velocity regime, using velocity histograms and power density (PD) diagrams, indicated that this site is not economically viable for the chosen tidal energy conversion method. This suggests the need for further experimentation and exploration of more efficient technologies, such as tidal kites.

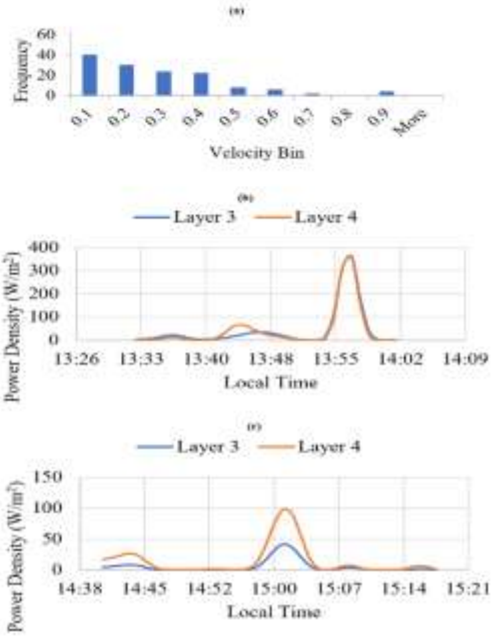

Figure 9. Site velocity histogram and PD: (a) velocity histogram for layers 3 and 4, (b) PD for layers 3 and 4 in time section A, and (c) PD for layers 3 and 4 in time section B.

Declaration of competing interest

The authors declare that they have no known competing financial interests or personal relationships that could have appeared to influence the work reported in this paper.

Acknowledgment

The authors would like to thank Dr. Noriaki Gohda and Prof. Arata Kaneko of Hiroshima University/Aqua Environmental Monitoring Limited Liability Partnership (AEM- LLP) for their strong support in constructing the CAT system.

Funding: This study was funded by Infrasound Research Laboratory (IRL) through grant No. IRL-TMO-1-202.

References

Bahaj, A. S. (2013). Marine current energy conversion: the dawn of a new era in electricity production. *Philosophical Transactions of the Royal Society A: Mathematical, Physical and Engineering Sciences*, *371*(1985), 20120500. https://doi.org/10.1098/rsta.2012.0500

Bahreinimotlagh, M., Kawanisi, K., Kavousi, A., Roozbahani, R., & Abbasi, M. (2020). Influence of Suspended Sediment Concentration and Particle Sizes on the Sound Attenuation of the Fluvial Acoustic Tomography Technique. *Journal of Water and Environment Technology*, *18*(5), 338–348. https://doi.org/10.2965/jwet.20-024

Gunawan, B., Neary, V. S., & Colby, J. (2014). Tidal energy site resource assessment in the East River tidal strait, near Roosevelt Island, New York, New York. *Renewable Energy*, *71*, 509–517. https://doi.org/10.1016/j.renene.2014.06.002

Huang, H., Guo, Y., Li, G., Arata, K., Xie, X., & Xu, P. (2020). Short-range water temperature profiling in a lake with coastal acoustic tomography. *Sensors (Switzerland)*, *20*(16), 1–14. https://doi.org/10.3390/s20164498

Jahromi, M. S. (2024). Tidal components along the north of Oman Gulf and Persian Gulf. *International Journal of Coastal, Offshore and Environmental Engineering*, *8*(4), 36–48.

Kaneko, A., Zhu, X.-H., & Lin, J. (2020). Coastal Acoustic Tomography. In *Elsevier*. Elsevier. https://doi.org/10.1016/B978-0-12-818507-0.00005-6

Kawanishi, K., BahrainiMotlagh, M., & Razaz, M. (2015). Energy flux measurement of tidal stream in a strait using two crossing ultrasonic transmission lines. *36th World Congress of the International Association of Hydro-Environment Engineering and Research (IAHR-APD 2015)*, 1–4.

khoshkholgh, A. (2023). Applying and Assessing the Performance of Projection Method in External Mode of Princeton Ocean Model by Simulating Tidal Currents in the Persian Gulf. *International Journal Of Coastal, Offshore And Environmental Engineering(Ijcoe)*, *8*(3), 22–31. https://doi.org/10.22034/ijcoe.2023.399301.1033

Li, G. (2018). *Flow velocity mapping in a circular experimental wave / current basin with small scale underwater acoustic tomography method* (Issue June). University of Edinburgh.

Li, G., Ingram, D., Kaneko, A., Chen, M., Gohda, N., & Polydorides, N. (2017). Vertical underwater acoustic tomography in an experimental basin. *The Journal of the Acoustical Society of America*, *141*(5), 3656–3656. https://doi.org/10.1121/1.4987918

Radfar, S., Panahi, R., Javaherchi, T., Filom, S., & Mazyaki, A. R. (2017). A comprehensive insight into tidal stream energy farms in Iran. In *Renewable and Sustainable Energy Reviews* (Vol. 79, pp. 323–338). Elsevier Ltd. https://doi.org/10.1016/j.rser.2017.05.037

Roberts, A., Thomas, B., Sewell, P., Khan, Z., Balmain, S., & Gillman, J. (2016). Current tidal power technologies and their suitability for applications in coastal and marine areas. *Journal of Ocean Engineering and Marine Energy*, *2*(2), 227–245. https://doi.org/10.1007/s40722-016-0044-8

Sellar, B., & Wakelam, G. (2018). Characterisation of Tidal Flows at the European Marine Energy Centre in the Absence of Ocean Waves. *Energies*, *11*(1), 176. https://doi.org/10.3390/en11010176

Syamsudin, F., Chen, M., Kaneko, A., Adityawarman, Y., Zheng, H., Mutsuda, H., Hanifa, A. D., Zhang, C., Auger, G., Wells, J. C., & Zhu, X. (2017). Profiling measurement of internal tides in Bali Strait by reciprocal sound transmission. *Acoustical Science and Technology*, *38*(5), 246–253. https://doi.org/10.1250/ast.38.246

Syamsudin, F., Taniguchi, N., Zhang, C., Hanifa, A. D., Li, G., Chen, M., Mutsuda, H., Zhu, Z., Zhu, X., Nagai, T., & Kaneko, A. (2019). Observing Internal Solitary Waves in the Lombok Strait by Coastal Acoustic Tomography. *Geophysical Research Letters*, *46*(17–18), 10475–10483. https://doi.org/10.1029/2019gl084595

Taniguchi, N., Huang, C.-F., Kaneko, A., Liu, C.-T., Howe, B. M., Wang, Y.-H., Yang, Y., Lin, J., Zhu, X.-H., & Gohda, N. (2013). Measuring the Kuroshio Current with ocean acoustic tomography. *The Journal of the Acoustical Society of America*, *134*(4), 3272–3281. https://doi.org/10.1121/1.4818842

Taniguchi, N., Takahashi, T., Yoshiki, K., Yamamoto, H., Hanifa, A. D., Sakuno, Y., Mutsuda, H., Huang, S. W., Huang, C. F., & Guo, J. H. (2021). A reciprocal acoustic transmission experiment for precise observations of tidal currents in a shallow sea. *Ocean Engineering*, *219*(June), 108292. https://doi.org/10.1016/j.oceaneng.2020.108292

Thiébaut, M., Filipot, J.-F., Maisondieu, C., Damblans, G., Jochum, C., Kilcher, L. F., & Guillou, S. (2020). Characterization of the vertical evolution of the three-dimensional turbulence for fatigue design of tidal turbines. *Philosophical Transactions of the Royal Society A: Mathematical, Physical and Engineering Sciences*, *378*(2178), 20190495. https://doi.org/10.1098/rsta.2019.0495